

# Antiperovskite $\text{Gd}_3\text{SnC}$ : Unusual Coexistence of Ferromagnetism and Heavy Fermions in Gd Lattice

Joonho Bang, Jongho Park, Kimoon Lee, Minsoo Kim, Wonshik Kyung, Jonathan D. Denlinger, Yeongkwan Kim, Young Hee Lee, Changyoung Kim,\* and Sung Wng Kim\*

Inverted structures of common crystal lattices, referred to as antistructures, are rare in nature due to their thermodynamic constraints imposed by the switched cation and anion positions in reference to the original structure. However, a stable antistructure formed with mixed bonding characters of constituent elements in unusual valence states can provide unexpected material properties. Here, a heavy-fermion behavior of ferromagnetic gadolinium lattice in  $\text{Gd}_3\text{SnC}$  antiperovskite is reported, contradicting the common belief that ferromagnetic gadolinium cannot be a heavy-fermion system due to the deep energy level of localized 4f-electrons. The specific heat shows an unusually large Sommerfeld coefficient of  $\approx 1114 \text{ mJ mol}^{-1} \text{ K}^{-2}$  with a logarithmic behavior of non-Fermi-liquid state. It is demonstrated that the heavy-fermion behavior in the non-Fermi-liquid state appears to arise from the hybridized electronic states of gadolinium 5d-electrons participating in metallic Gd–Gd and covalent Gd–C bonds. These results accentuate the unusual chemical bonds in  $\text{CGd}_6$  octahedra with the dual characters of gadolinium 5d-electrons for the emergence of heavy fermions.

cations and anions from the original structure often have a reversed compositional ratio, which necessarily forms a different coordinated substructure with additional bonding characters and can lead to an exotic electronic structure. However, in general, such antistructures composed of the same constituent elements in the reversed compositional ratio are thermodynamically unstable. Indeed, due to the thermodynamic constraints, antistructures found in several classes of materials are constructed by subsidiary chemical bonds of different constituent elements from original structures. This appears, for example, in the Cd-deficient  $\text{Cd}_3\text{As}_2$  antiferrofluorite,<sup>[1]</sup> which has a strong covalent bonding nature in a reversed compositional ratio from the ionic  $\text{CaF}_2$  fluorite. It is noteworthy that the  $\text{Cd}_3\text{As}_2$  antiferrofluorite exhibits exotic properties: a 3D topological Dirac band<sup>[1]</sup> along with negative magnetoresistance,<sup>[2]</sup> anomalous Hall effect,<sup>[3]</sup> and pressure-induced superconductivity.<sup>[4]</sup>

## 1. Introduction

The crystal structure constructed with chemical bonds of constituent elements determines the electronic structure of a material and its properties. In a fixed symmetry, electronically inverted structures with switched crystallographic positions of

ABX<sub>3</sub> perovskites, as the largest family of crystalline materials, also have their counterpart antistructures, A<sub>3</sub>BX antiperovskites.<sup>[5]</sup> In contrast to the perovskite compounds constructed by the ionic bonds of constituent elements in stable

Prof. J. Bang, Dr. J. Park, Prof. S. W. Kim  
Department of Energy Science  
Sungkyunkwan University  
Suwon 16419, Republic of Korea  
E-mail: kimsungwng@skku.edu

Prof. K. Lee  
Department of Physics  
Kunsan National University  
Gunsan 54150, Republic of Korea

M. Kim, Dr. W. Kyung, Prof. C. Kim  
Center for Correlated Electron Systems  
Institute for Basic Science  
Seoul 08826, Republic of Korea  
E-mail: changyoung@snu.ac.kr

M. Kim, Dr. W. Kyung, Prof. C. Kim  
Department of Physics and Astronomy  
Seoul National University  
Seoul 08826, Republic of Korea

Dr. J. D. Denlinger  
Advanced Light Source  
Lawrence Berkeley National Laboratory  
Berkeley, CA 94720, USA

Prof. Y. Kim  
Department of Physics  
Korea Advanced Institute of Science and Technology  
Daejeon 34141, Republic of Korea

Prof. Y. Kim  
Graduate School of Nanoscience and Technology  
Korea Advanced Institute of Science and Technology  
Daejeon 34141, Republic of Korea

Prof. Y. H. Lee, Prof. S. W. Kim  
Center for Integrated Nanostructure Physics  
Institute for Basic Science  
Suwon 16419, Republic of Korea

The ORCID identification number(s) for the author(s) of this article can be found under <https://doi.org/10.1002/adma.202102958>.

DOI: 10.1002/adma.202102958

valence states, the antiperovskites have mixed bonding characters with ionic, covalent, and metallic bonds in unusual valence states.<sup>[6]</sup> However, oxide antiperovskites ( $A_3BO$ ), antistructures of common oxide perovskites ( $ABO_3$ ), are hardly stabilized in ambient conditions as oxygen tends to form ionic bonds with countercationic A and B elements due to its large ionicity.<sup>[7]</sup> This constraint may be lifted for s-block and transition-metal-based antiperovskites, in which additional covalent and metallic bonds come into play for their crystallographic stability.<sup>[5,8]</sup> The boundary for such stable antiperovskite compounds can be extended to f-block lanthanides, which form a crystal with various elemental groups of d-block transition metals and p-block post-transition metals.<sup>[5]</sup> Those compounds may exhibit diverse electronic properties because of the multiple bonding characters with enhanced covalency and/or metallicity. Furthermore, considering the fact that f-electrons often contribute to strongly correlated electronic properties, a variety of unconventional quantum phenomena may be anticipated in f-block antiperovskites, which can exhibit exotic electronic band structures arising from the mixed chemical bonds. However, thermodynamically stable f-block-element-based antiperovskites and their novel properties have been hardly demonstrated up to now.<sup>[5,9]</sup> Herein, we demonstrate the unprecedented heavy-fermion behavior of the ferromagnetic (FM) gadolinium lattice in the  $Gd_3SnC$  antiperovskite structure and verify the crucial role of the metallic Gd–Gd and covalent Gd–C bonds of  $CGd_6$  octahedral skeleton on an unusually hybridized Gd 5d-electrons responsible for the emergent heavy fermions.

## 2. Results and Discussion

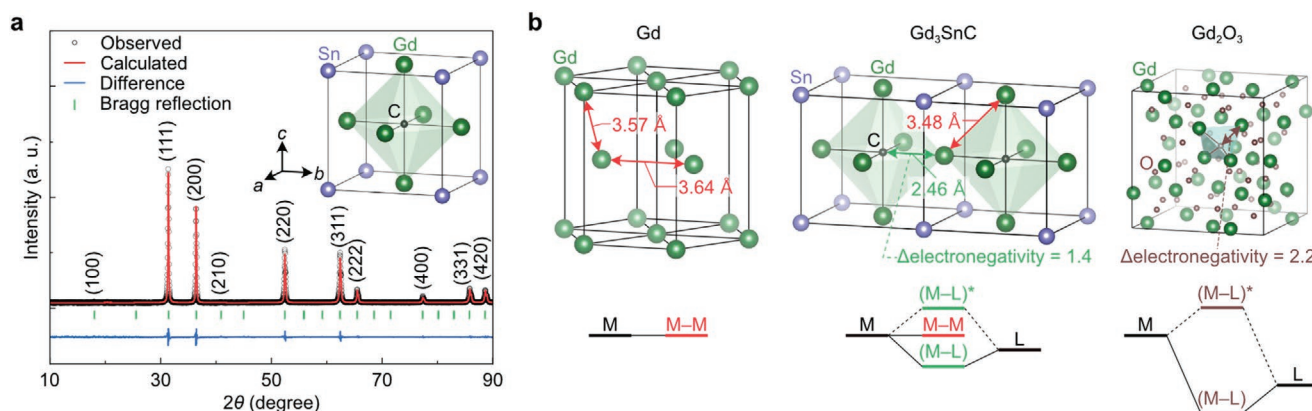
### 2.1. Synthesis and Structural Analysis

Figure 1a shows that the  $Gd_3SnC$  crystallizes in the antiperovskite structure (space group:  $Pm\bar{3}m$ ) with face-centered Gd and body-centered C atoms in a Sn cubic lattice, as confirmed

by Rietveld analysis of powder X-ray diffraction (XRD) pattern (Table S1, Supporting Information). Single-phase bulk  $Gd_3SnC$  was synthesized via the melt-solidification process at one atmosphere. This indicates the thermodynamic stability of  $Gd_3SnC$  antiperovskite, which gets additional support from the calculated phonon dispersions having no imaginary frequency (Figure S1, Supporting Information). In contrast to the  $ABX_3$  perovskite, which has cation-centered  $BX_6$  octahedra with ionic bonds,  $Gd_3SnC$  has anion-centered  $CGd_6$  octahedra with strong covalent Gd–C and metallic Gd–Gd bonds. This mixed bonding character of Gd bonds in  $CGd_6$  octahedra results in different Gd orbital levels from those of the Gd element and its ionic compounds. As shown in Figure 1b, while Gd metal and  $Gd_2O_3$  have ordinary Gd orbital levels of Gd–Gd metallic and Gd–O ionic bonds, respectively,  $Gd_3SnC$  has unusual energy levels for Gd orbitals due to the coexistence of metallic and covalent bonds. Considering the shorter Gd–Gd bond length (3.48 Å) in  $CGd_6$  octahedra compared to that of Gd metal ( $\approx 3.6$  Å), one expects an enhanced metallicity and thus additional Fermi level ( $E_F$ ) crossings for Gd bands in  $Gd_3SnC$ . On the other hand, the electronegativity difference between Gd and C is much smaller than that between Gd and O, resulting in the formation of covalent bonds between Gd and C. The energy difference between bonding and antibonding states of the covalent bonds is expected to be significantly smaller than that of ionic bonds between Gd and O. These mixed bonding characters of Gd valence orbitals in  $CGd_6$  octahedra can lead to a peculiar molecular orbital diagram with both metallic and covalent bonds, as shown in Figure 1b. Such observation indicates that  $Gd_3SnC$  antiperovskite may exhibit unusual physical properties that are hardly found in elemental Gd and conventional Gd-related compounds.

### 2.2. Tricritical Ferromagnetic Behavior

Figure 2a shows the FM phase transition of  $Gd_3SnC$  with a Curie temperature ( $T_C$ ) of 100 K under a low magnetic field ( $H$ )



**Figure 1.** Crystal structure and mixed bonding nature of  $Gd_3SnC$  antiperovskite. a) Powder XRD pattern with Rietveld fitting of  $Gd_3SnC$ . The measurement was performed at room temperature. The inset depicts the crystal structure obtained from the Rietveld refinement result. b) Comparison of bonding features in Gd-based compounds. The red, green, and brown colors represent the metallic Gd–Gd (M–M), covalent Gd–ligand (M–L), and ionic Gd–ligand (M–L) bonds, respectively. The bond lengths of the Gd–Gd and Gd–C bonds, and the electronegativity difference ( $\Delta$ electronegativity) between Gd and the surrounding ligands are also shown in the crystal structures. Schematics of molecular orbital diagrams are shown in the lower panel. (M–L)\* represents the antibonding molecular orbital of M–L bonds. The relative energy difference between bonding and antibonding molecular orbitals of Gd–C bond is estimated to be  $\approx 9$  eV (details are provided in Figure S2 in the Supporting Information).

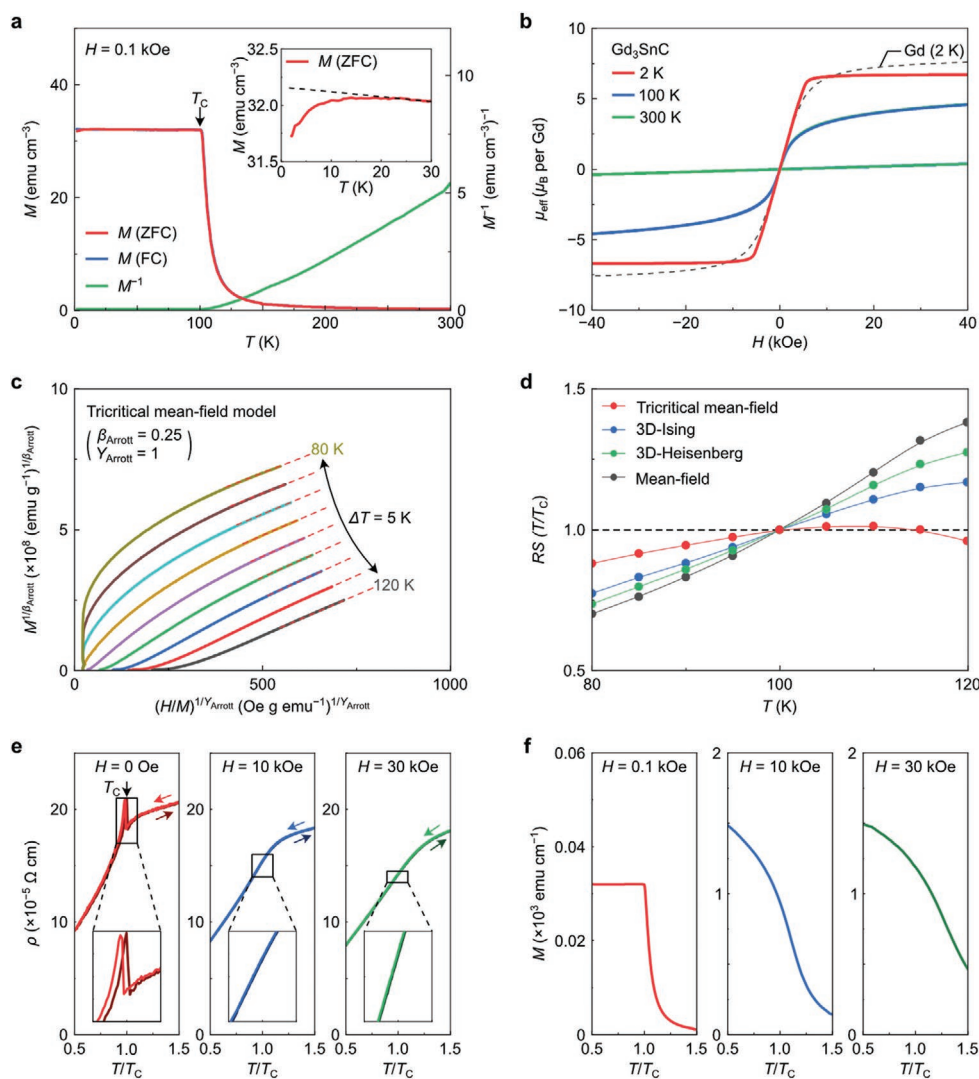


**Figure 2.** Tricritical ferromagnetic behavior in  $\text{Gd}_3\text{SnC}$  antiperovskite. a)  $T$ -dependent  $M$  under zero-field cooling (ZFC) and field cooling (FC) conditions. Inverse magnetization ( $M^{-1}$ ) for FC result is also illustrated. The inset shows an enlarged view of the ZFC curve at low  $T$ . The dashed black line is a guide for the eyes. b)  $H$ -dependent effective magnetic moment ( $\mu_{\text{eff}}$ ) per Gd atom at various  $T$ . The  $\mu_{\text{eff}}-H$  curve for Gd metal obtained at 2 K is also shown as a reference (dashed black curve). c) Modified Arrott plot for the tricritical mean-field model. Modified Arrott plots for other models are presented in Figure S3a–d (Supporting Information). The dashed red lines are linear fits for the high field regime. d)  $T$ -dependent relative slope (RS) curves near the  $T_C$  for various models. e) Cooling and heating curves of  $T$ -dependent  $\rho$  for various  $H$  values. f)  $M-T$  curves for various  $H$  values.

of 0.1 kOe. In comparison to the itinerant FM in Gd metal with a  $T_C$  of 297 K, different aspects of the FM order are observed.<sup>[10]</sup> A sharp increase in the magnetization ( $M$ ) near the  $T_C$  indicates a first-order transition, which is further evidenced by the hysteresis in the temperature ( $T$ ) dependence of electrical resistivity ( $\rho$ ) (Figure 2e) and the negative slope in the  $M^2$  dependence of  $H/M$  (Figure S3e, Supporting Information). In addition, a sharp anomaly in the lattice parameter  $a$  is observed around the  $T_C$ , which should be due to the first-order nature of the phase transition. However, no symmetry change such as lattice distortion is observed, indicating that the antiperovskite structure is preserved across the FM ordering (Figure S4, Supporting Information). We confirm the saturation magnetic moment of  $\approx 6.8 \mu_B$  per Gd obtained from the  $M-H$  curve (Figure 2b), indicating this FM state comes mostly from the seven Gd

4f-electrons. A notable aspect of  $M(T)$  is a slight decrease in the zero-field cooling (ZFC) curve below  $\approx 20$  K (inset of Figure 2a). Considering the fact that the magnetic contribution of the heat capacity from the heavy-fermion state appears below  $\approx 20$  K (Figure 3c,d), this magnetic suppression can be possibly attributed to the spin reorientation such as Kondo singlet formation,<sup>[11,12]</sup> as will be discussed in the following sections. This unusual behavior in  $M$  indicates that the near  $E_F$  states of Gd, which do not have contributions from fully localized f-orbitals, may be different from those of the familiar FM Gd metal and Gd-based compounds.<sup>[10,13]</sup>

The most peculiar aspect of the FM state in  $\text{Gd}_3\text{SnC}$  is the tricritical behavior that appears near the boundary between the first- and the second-order phase transitions.<sup>[14]</sup> Figure 2c shows a modified Arrott plot<sup>[15]</sup> of the tricritical mean-field model for

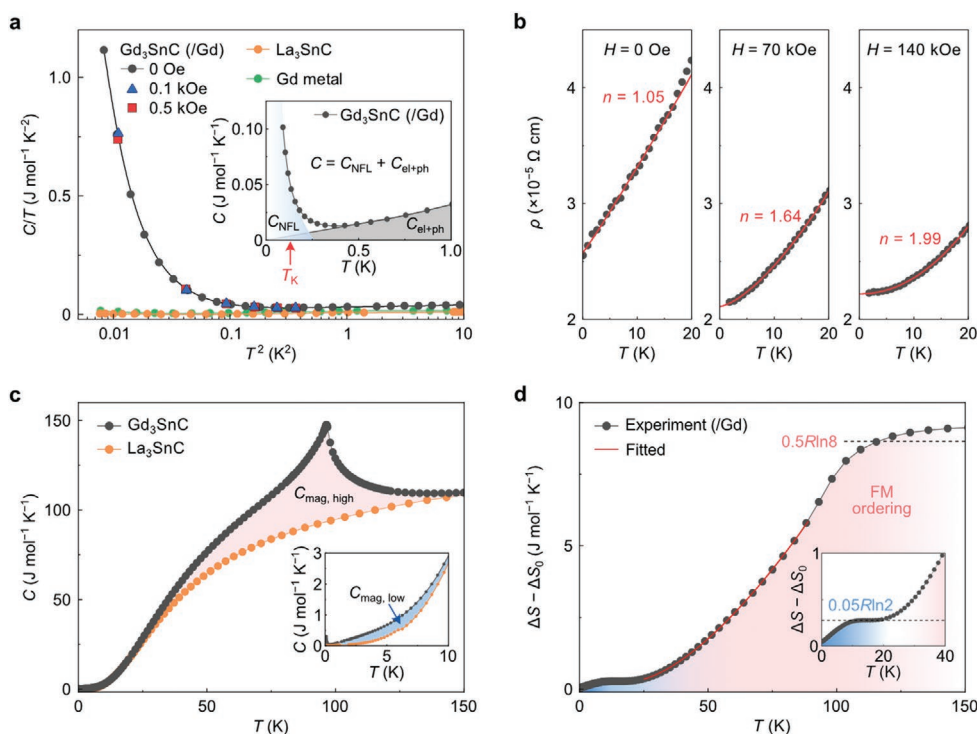


**Figure 3.** Unconventional heavy-fermion behavior with non-Fermi-liquid behavior in Gd<sub>3</sub>SnC antiperovskite. a)  $C/T$  versus  $T^2$  curves for antiperovskite Gd<sub>3</sub>SnC, isostructural La<sub>3</sub>SnC, and Gd metal. The  $C$  value of Gd<sub>3</sub>SnC corresponds to the heat capacity per mole of Gd. The inset shows a fitting result of  $C$  versus  $T$  curve of Gd<sub>3</sub>SnC using  $C_{\text{NFL}} = -u \ln(T/T_0) + \nu$  and  $C_{\text{el+ph}} = \omega T + \beta T^3$ , where  $C_{\text{NFL}}$  and  $C_{\text{el+ph}}$  are NFL and electron + phonon contributions, respectively.  $u$  ( $= 1.937$  mJ mol<sup>-1</sup> K<sup>-2</sup>),  $T_0$  ( $= 0.138$  K), and  $\nu$  ( $= 0.254$  mJ mol<sup>-1</sup> K<sup>-2</sup>) are constants, and  $\omega$  ( $= 34.180$  mJ mol<sup>-1</sup> K<sup>-2</sup>) and  $\beta$  ( $= 0.671$  mJ mol<sup>-1</sup> K<sup>-4</sup>) are electron contribution above  $T_K$  and phonon contributions, respectively. b)  $T$ -dependent  $\rho$  at different  $H$ . The red curves are single power-law fits ( $\rho = \rho_0 + AT^n$ ) of the data, where  $A$  is a constant. c)  $C$  versus  $T$  for Gd<sub>3</sub>SnC and La<sub>3</sub>SnC. The inset is an enlarged view of the low- $T$  region.  $C_{\text{mag}}$  for Gd<sub>3</sub>SnC is estimated by subtracting the  $C$  of the nonmagnetic La<sub>3</sub>SnC (Figure S5b, Supporting Information). d)  $T$ -dependent  $\Delta S - \Delta S_0$  for Gd<sub>3</sub>SnC per mole of Gd.  $\Delta S_0$  is the residual entropy. The red curve represents the FM contribution obeying  $\Delta S - \Delta S_0 = \int (C_{\text{mag}}/T) dT$ , where  $C_{\text{mag}} = (aT^{3/2} + b)$ .  $a$  ( $= 0.02$  J mol<sup>-1</sup> K<sup>-5/2</sup>) and  $b$  ( $= -2.50$  J mol<sup>-1</sup> K<sup>-1</sup>) are constants. The inset shows a magnified view below 40 K.

the FM order with  $\beta_{\text{Arott}} = 0.25$  and  $\gamma_{\text{Arott}} = 1$  in  $(H/M)^{1/\gamma_{\text{Arott}}}$  and  $M^{1/\beta_{\text{Arott}}}$ , respectively. Compared to other magnetic ordering models, it is apparent from the relative slopes (dashed red lines in Figure 2c and Figure S3a–d (Supporting Information)) that the FM transition belongs to the universality class of the tricritical mean-field model (Figure 2d). A clear crossover from a first-order to second-order transition is seen in the  $T$ -dependent  $\rho$  and  $M$  curves under different  $H$ , as shown in Figure 2e,f, respectively. Three representative features in the data verify the crossover between FM orders: i) disappearance of the peak in  $\rho$  at  $T_C$ , ii) suppression of the hysteresis in the  $\rho$ – $T$  curve during a thermal cycle (insets of Figure 2e) and iii) smooth increase of  $M$  upon cooling (Figure 2f). Such tricritical behavior often emerges in heavy-fermion systems such as UGe<sub>2</sub><sup>[16]</sup> and YbRh<sub>2</sub>Si<sub>2</sub><sup>[17]</sup> due to the competition between Kondo coupling ( $T_K$ ) and Ruderman–Kittel–Kasuya–Yosida interaction.<sup>[18]</sup>

### 2.3. Heavy Fermions with Non-Fermi-Liquid Behavior

More unusual properties of Gd<sub>3</sub>SnC may be found in the heat capacity ( $C$ ) measurement results (Figure 3). As a way to determine the unexpected behavior, we compare the  $C$  of Gd<sub>3</sub>SnC to those of FM Gd metal and nonmagnetic La<sub>3</sub>SnC

antiperovskite, as shown in Figure 3a. In contrast to the small  $C$  values of Gd metal and La<sub>3</sub>SnC antiperovskite in the low- $T$  region, an extremely large  $C$  value with a Sommerfeld coefficient ( $\gamma$ ) of  $\approx 1114$  mJ mol<sup>-1</sup> K<sup>-2</sup> at 90 mK is observed for the Gd<sub>3</sub>SnC. The dramatic low- $T$  rise of  $C$  is reminiscent of a nuclear Schottky anomaly, most likely from the Sn nucleus (the natural abundance for nonzero nuclear spin <sup>13</sup>C is below 1%). However, our modeling, which considers 16% natural abundance of <sup>117</sup>Sn and <sup>119</sup>Sn, rules out the Schottky anomaly by showing that the required internal field is about  $-1287$  kOe, a value much larger than any reported values<sup>[19–21]</sup> (Figure S5d, Supporting Information). In addition, the Gd nuclear spin cannot be the culprit as we do not see a similar rise in  $C$  for Gd metal. Therefore, we attribute the logarithmic rise of  $C$  for Gd<sub>3</sub>SnC below  $\approx 0.13$  K (Figure 4a) to a non-Fermi-liquid (NFL) behavior of itinerant conduction electrons<sup>[22–24]</sup> (inset of Figure 3a). A  $T$ -linear dependence of  $\rho$  in the low- $T$  region also supports the NFL behavior of itinerant conduction electrons in Gd<sub>3</sub>SnC (left panel in Figure 3b). The transition from  $T$ -linear to  $T^2$  behavior of  $\rho$  upon applying 140 kOe (right panel in Figure 3b and Figure S6 (Supporting Information)) is suggestive of a magnetic origin of the NFL behavior.<sup>[25,26]</sup> Thus, we assume that an exotic quantum phenomenon coupled with a correlation between itinerant and



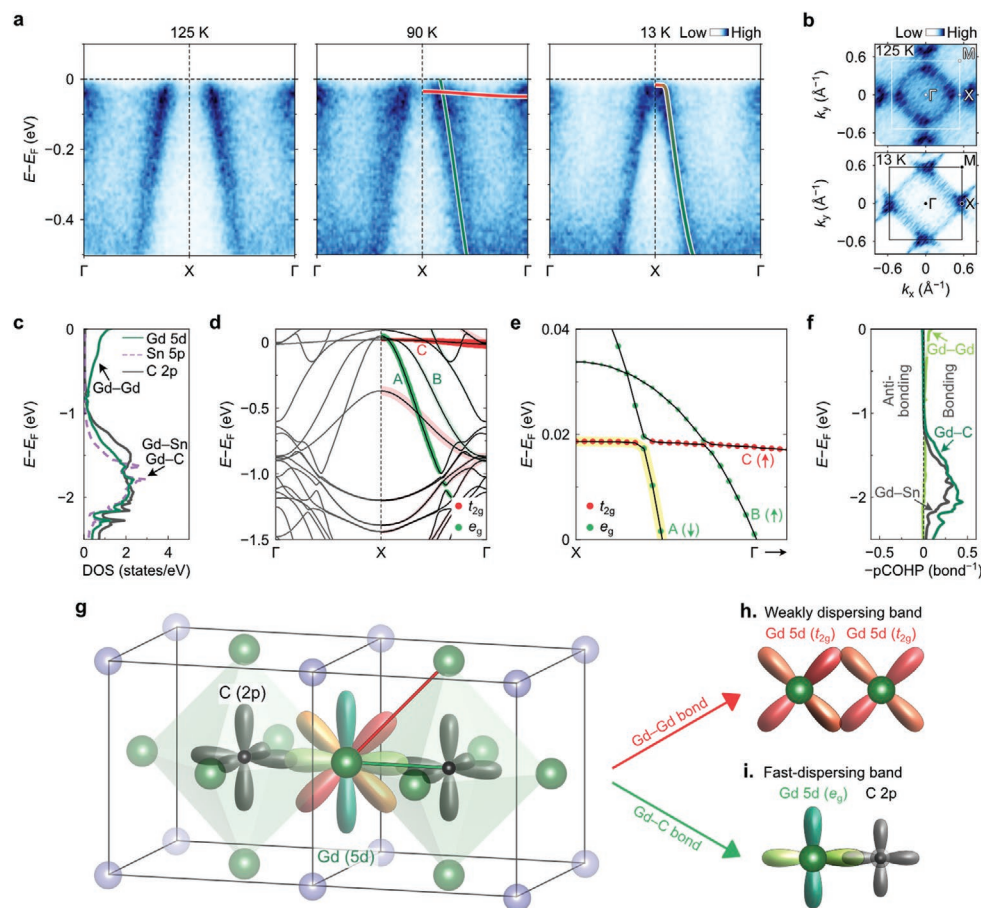


**Figure 4.** Electronic structure of heavy-fermion  $\text{Gd}_3\text{SnC}$  antiperovskite. a) ARPES spectra along the  $\Gamma$ -X- $\Gamma$ -direction at 125, 90, and 13 K. Green and red solid curves indicate fast-dispersing band and weakly dispersing band, respectively. Details on the energy distribution curves (EDCs) are shown in Figure S7 (Supporting Information). b) Fermi surface topology in the  $k_x$ - $k_y$ -plane from ARPES measurements at 125 and 13 K. The white and black squares represent the first Brillouin zone. c) Calculated partial DOS. d) Calculated band structure along the  $\Gamma$ -X- $\Gamma$ -direction with fat band analysis, exhibiting the  $t_{2g}$  (red color) and  $e_g$  (green color) contributions of Gd 5d-orbitals. Band thickness represents the contribution of each orbital. e) Near Fermi level band structure around the X point, showing a band hybridization between fast-dispersing and weakly dispersing bands. f) Partial COHP (pCOHP) for Gd-Gd, Gd-C, and Gd-Sn bonds. pCOHP for other bonds can be found in Figure S10 (Supporting Information). g-i) Schematic illustration of the mixed bonding state for Gd 5d-orbitals.

localized electrons in the  $\text{Gd}_3\text{SnC}$  antiperovskite appears as heavy fermions.

Considering that the NFL behavior of Gd 5d electrons occurs in the presence of heavy-fermion state, the NFL behavior in our system is different from the NFL behavior in the conventional f-electron systems that often appeared in the vicinity of a quantum critical point where the magnetic phase transition is suppressed to zero temperature. Instead, the coexistence of heavy-fermion state and NFL behavior observed in  $\text{Gd}_3\text{SnC}$  is analogous to the unconventional multichannel Kondo system with the overcompensated situation ( $n > 2S$ , where  $n$  and  $S$  are the numbers of conduction electron channels and localized spins, respectively).<sup>[23]</sup>

As Gd f-electron levels locate deep in the binding energy, the heavy fermion with the NFL behavior should originate from the electrons of other orbitals, which is revealed from the analysis of the  $C$  of FM  $\text{Gd}_3\text{SnC}$ . The magnetic contribution ( $C_{\text{mag}}$ ) to the  $C$  of FM  $\text{Gd}_3\text{SnC}$  is obtained by subtracting the  $C$  of nonmagnetic  $\text{La}_3\text{SnC}$  without 4f-electrons (La metal

with the configuration of  $[\text{Xe}]4f^05d^16s^2$ ) from those of  $\text{Gd}_3\text{SnC}$  with seven 4f-electrons (Gd metal with the configuration of  $[\text{Xe}]4f^75d^16s^2$ ). We find two distinct features in  $C_{\text{mag}}$ : a large  $C_{\text{mag}}$  in the high- $T$  region ( $C_{\text{mag,high}}$ , Figure 3c) and a small  $C_{\text{mag}}$  in the low- $T$  region ( $C_{\text{mag,low}}$ , inset of Figure 3c). While the  $C_{\text{mag,high}}$  is attributed to the FM order of  $4f^7$ -electrons, which agrees well with the prediction of the renormalization-group approach<sup>[27]</sup> in the scheme of tricritical ferromagnetism (Figure S3f, Supporting Information), the origin of  $C_{\text{mag,low}}$  is ambiguous. From the  $T$ -dependent magnetic entropy ( $\Delta S$ ) obtained by integrating  $C_{\text{mag}}(T)$  (Figure S5b, Supporting Information), we can assign which electrons are responsible for  $C_{\text{mag,low}}$ . Figure 3d shows a large difference in  $\Delta S$  between the high- and low- $T$  regions:  $0.5R\ln 8$  and  $0.05R\ln 2$ , respectively. Since  $0.5R\ln 8$  reflects the contribution from seven 4f-electrons ( $4f^7$ ) involved in FM ordering, one may notice that the much smaller value of  $0.05R\ln 2$  has no correlation with 4f-electrons but is ascribed to 5d-electrons, which are responsible for the heavy fermion with the NFL behavior.

## 2.4. Dual Character of Gd 5d-Electrons

This unconventional and anomalous d-electron heavy-fermion state in f-block Gd-based  $\text{Gd}_3\text{SnC}$  is, if true, the first case of FM-assisted heavy-fermion behavior in 5d-electron systems. Density functional theory (DFT) calculations along with angle-resolved photoemission spectroscopy (ARPES) measurements provide a clear picture for the formation of the heavy-fermion state, which is induced not by 4f-electrons but by 5d-electrons of Gd element in the context of mixed bonding characters of the antiperovskite structure. Figure 4a shows ARPES data along the  $\Gamma$ -X- $\Gamma$ -direction taken above (125 K) and below (90 and 13 K) the  $T_C$ . The 125 K data show a fast-dispersing band centered at the X point. As the  $T$  is lowered to 90 K, the band shifts down due to the exchange splitting of both 4f- and 5d-electrons (Figure S7d, Supporting Information). In addition to the fast-dispersing band (green curve), there is a weakly dispersing band near  $E_F$  (red curve in Figure 4a, Figure S7a–c (Supporting Information)). Upon cooling to 13 K, the fast-dispersing band shifts further down, and the weakly dispersing band near  $E_F$  disappears. These changes in the electronic structure might be related to the hybridization of fast and weakly dispersing bands below 20 K. The  $T$ -dependent electronic structure change is also seen in the  $k_x$ - $k_y$ -plane of Fermi surface maps in Figure 4b; the Fermi surface pocket becomes larger as the  $T$  decreases. This enlarged Fermi surface is attributed to FM-ordering-induced electronic structure change near the  $E_F$  with a possible additional contribution from localized spins to the  $E_F$  due to the formation of Kondo singlets.<sup>[25,28–30]</sup> The calculated partial density of states (DOS) clearly demonstrates that the Gd 5d-orbitals are almost solely responsible for the states near  $E_F$ , while Sn 5p- and C 2p-derived states are located away from  $E_F$  (Figure 4c). Meanwhile, we confirm that the contribution of Gd 4f-orbitals into the band structure near  $E_F$  is negligible but responsible for the FM ordering (Figures S8 and S9, Supporting Information).

We note that the calculated band structure shows an anomalous flat band feature near  $E_F$ , which is also a signature of heavy-fermion behavior (Figure 4d,e). The experimentally observed flatness of the fast-dispersing band at the X point (13 K in Figure 4a) is indeed well-reproduced by band calculations (highlighted as yellow color in Figure 4e). The flat band analysis reveals that the band hybridization triggers the appearance of a flat band feature near  $E_F$ . Importantly, the two hybridized bands originate from the only Gd 5d-orbitals:  $t_{2g}$  bands from the Gd–Gd bonds (red curves) and  $e_g$  bands from mostly the Gd–C bonds (green curves). Thus, we believe that the flat  $t_{2g}$  band observed at 90 K (Figure 4a) is lifted above  $E_F$  after the band hybridization process (Figure S7e, Supporting Information). Finally, we emphasize the importance of antiperovskite structure with mixed bonding nature, which is the key to imparting the unusual heavy-fermion behavior to  $\text{Gd}_3\text{SnC}$ . The crystal orbital Hamiltonian population (COHP) analysis (Figure 4f) explains how the chemical bonds of  $\text{CGd}_6$  octahedra in antiperovskite structure can induce the unusual band structure. The COHP analysis suggests two types of orbital overlap: a small orbital overlap in metallic Gd–Gd bond responsible for the  $t_{2g}$  bands near  $E_F$  (ICOHP  $\approx 0.5$  eV per bond, Table S2 (Supporting Information), where ICOHP is integrated crystal orbital Hamiltonian population) and large orbital overlap in covalent

Gd–C bond for the  $e_g$  bands below  $E_F$  (ICOHP  $\approx 1.5$  eV per bond). This mixed bonding nature with the different degrees of orbital overlap leads to the unusual band dispersion of Gd 5d-electrons, as illustrated in Figure 4g–i. Thus, the duality of Gd 5d-electrons participating in the mixed chemical bonds in  $\text{CGd}_6$  octahedra of the  $\text{Gd}_3\text{SnC}$  antiperovskite structure is a key factor that determines the unusual physical properties.

## 3. Conclusions

We have discovered the d-electron heavy-fermion state in the f-electron FM  $\text{Gd}_3\text{SnC}$  antiperovskite. The mixed bonding nature of the antiperovskite structure, composed of metallic Gd–Gd bonds and covalent Gd–C bonds, is found to be the key ingredient for realizing the heavy fermions of Gd 5d-electrons. The unusual coexistence of FM and heavy fermions in Gd lattice originating from the dual character of Gd electrons shows that the antiperovskite structure can be a new platform for the study of a novel class of strongly correlated electron systems in which the localized and itinerant electrons impart different physical properties. Furthermore, the family of  $\text{Ln}_3\text{SnC}$  (Ln: Lanthanides) antiperovskite can give the freedom of manipulating the mixed bonding nature by an isovalent substitution and provide an opportunity to discover intriguing heavy-fermion systems with unconventional superconductivity<sup>[31,32]</sup> or high thermoelectric power.<sup>[33,34]</sup> Finally, it is highlighted that the present findings are against the knowledge that the FM lanthanide elements are not suitable for heavy-fermion states, implying that the antistructured lattice framework may manifest novel physical properties completely unexpected in the common crystal structure. This work will trigger further exploratory studies on antistructures to challenge the common knowledge in the elemental properties of materials.

## 4. Experimental Section

**Crystal Growth and Structural Analysis:** Stoichiometric polycrystalline  $\text{Gd}_3\text{SnC}$  ingot rods were used for the single-crystal growth by the floating zone (FZ) melting method. Gd metal, Sn metal, and graphite chips were mixed in a 3:1:1 molar ratio to fabricate a polycrystal ingot rod. The mixed sample was melted using the arc melting furnace in a high-purity argon atmosphere (Ar > 99.9999%). The single crystal was grown by a four-mirror FZ melting method with the rod-shaped ingots under high-purity argon (Ar > 99.9999%) with pressurized conditions in 0.3 MPa. The feed and seed rods were rotated at 50 rpm, and the growing speed was 2 mm h<sup>−1</sup>. The crystal structure was determined using the high-resolution X-ray diffractometer and Rietveld analysis using the GSAS-II program.<sup>[35]</sup>

**Physical Property Measurements:**  $\rho$ ,  $M$ , and  $C$  measurements were performed using a physical property measurement system (PPMS). The  $\rho$  and  $C$  at ambient pressure were measured down to 0.06 K using a diluted helium-3 refrigerator. To measure the electrical properties of samples, the electrical contacts in the four-probe configuration were adopted onto a sample using the Ag epoxy. To prevent movement of samples by  $H$  (up to 140 kOe) in the chamber, samples were fixed using Torr Seal epoxy onto the PPMS puck. To measure the  $M$  of the sample, a vibrating sample magnetometer was used. For  $C$  measurement, the standard relaxation method was adopted. Every process was performed in an Ar-filled glove box, and N-grease covered samples for  $\rho$  and  $C$  measurements to prevent degradation of  $\text{Gd}_3\text{SnC}$  under ambient oxygen and water vapor atmosphere.  $T$ -dependent ARPES measurements were

performed at the MERLIN beamline (BL) 4.0.3 of the Advanced Light Source, Lawrence Berkeley National Laboratory using both linearly horizontal ( $\pi$ ) and vertical ( $\sigma$ ) polarization from an elliptically polarized undulator. Spectra were acquired with a Scienta R8000 (BL 4.0.3) electron analyzer. Cleaving of the samples was conducted at 13 K in an ultrahigh vacuum better than  $5 \times 10^{-11}$  Torr. The total energy resolution of  $\approx 15$  meV was used for measurements at  $h\nu = 142$  eV.

**DFT Calculations:** First-principle DFT calculations were performed using the generalized gradient approximation with the Perdew–Burke–Ernzerhof functional with spin–orbit coupling and the projector augmented plane-wave method implemented in the Vienna Ab initio Simulation Package (VASP) program code.<sup>[36–38]</sup> The 4f-, 5s-, 5p-, 5d-, and 6s-electrons of Gd, the 5s- and 5p-electrons of Sn, and the 2s- and 2p-electrons of C were used as valence electrons. The plane-wave-basis cutoff energy was set to 600 eV. On-site Coulomb interaction values of  $U = 3$  eV were used for the Gd 5d-electrons (Figure S9, Supporting Information). Self-consistency was carried out using an  $a \times b \times c$  unit cell containing five atoms, and a  $12 \times 12 \times 12$   $k$ -point mesh was used. Structural relaxation was performed until the Hellmann–Feynman forces were less than  $1 \times 10^{-5}$  eV  $\text{\AA}^{-1}$ , respectively. The crystal structures and charge density distribution were visualized with the Visualization for Electronic and Structural Analysis code.<sup>[39]</sup>

## Supporting Information

Supporting Information is available from the Wiley Online Library or from the author.

## Acknowledgements

J.B. and J.P. contributed equally to this work. This work was supported by the Institute for Basic Science (Grant Nos. IBS-R011-D1, IBS-R009-G2) and the National Research Foundation of Korea (NRF) grant funded by the Korean government (Ministry of Science, ICT & Future Planning) (Nos. 2015M3D1A1070639, NRF-2019R111A1A01061913). The authors acknowledge Dr. Filip Ronning (Los Alamos National Laboratory) for valuable discussions.

## Conflict of Interest

The authors declare no conflict of interest.

## Data Availability Statement

The data that support the findings of this study are available from the corresponding author upon reasonable request.

## Keywords

antiperovskites, ferromagnetism, heavy fermions, non-Fermi-liquids, tricritical behavior

Received: April 19, 2021  
Revised: June 8, 2021  
Published online: July 28, 2021

- [1] S. Jeon, B. B. Zhou, A. Gyeon, B. E. Feldman, I. Kimchi, A. C. Potter, Q. D. Gibson, R. J. Cava, A. Vishwanath, A. Yazdani, *Nat. Mater.* **2014**, *13*, 851.

- [2] T. Liang, Q. Gibson, M. N. Ali, M. Liu, R. J. Cava, N. P. Ong, *Nat. Mater.* **2015**, *14*, 280.  
[3] M. Uchida, T. Koretsune, S. Sato, M. Kriener, Y. Nakazawa, S. Nishihaya, Y. Taguchi, R. Arita, M. Kawasaki, *Phys. Rev. B* **2019**, *100*, 245148.  
[4] L. He, Y. Jia, S. Zhang, X. Hong, C. Jin, S. Li, *npj Quantum Mater.* **2016**, *1*, 16014.  
[5] Y. Wang, H. Zhang, J. Zhu, X. Lü, S. Li, R. Zou, Y. Zhao, *Adv. Mater.* **2020**, *32*, 1905007.  
[6] D. Huang, H. Nakamura, K. Küster, A. Yaresko, D. Samal, N. B. M. Schröter, V. N. Strocov, U. Starke, H. Takagi, *Phys. Rev. Mater.* **2019**, *3*, 124203.  
[7] Y. Ma, A. Edgeton, H. Paik, B. D. Faeth, C. T. Parzyck, B. Pamuk, S.-L. Shang, Z.-K. Liu, K. M. Shen, D. G. Schlom, C.-B. Eom, *Adv. Mater.* **2020**, *32*, 2000809.  
[8] V. V. Bannikov, I. R. Shein, A. L. Ivanovskii, *Comput. Mater. Sci.* **2010**, *49*, 457.  
[9] T. M. Gesing, K. H. Wachtmann, W. Jeitschko, Z. *Naturforsch., B: J. Chem. Sci.* **1997**, *52*, 176.  
[10] H. E. Nigh, S. Legvold, F. H. Spedding, *Phys. Rev.* **1963**, *132*, 1092.  
[11] A. Steppke, R. Kuchler, S. Lausberg, E. Lengyel, L. Steinke, R. Borth, T. Luhmann, C. Krellner, M. Nicklas, C. Geibel, F. Steglich, M. Brando, *Science* **2013**, *339*, 933.  
[12] C. Krellner, S. Lausberg, A. Steppke, M. Brando, L. Pedrero, H. Pfau, S. Tencé, H. Rosner, F. Steglich, C. Geibel, *New J. Phys.* **2011**, *13*, 103014.  
[13] S. Y. Lee, J.-Y. Hwang, J. Park, C. N. Nandadasa, Y. Kim, J. Bang, K. Lee, K. H. Lee, Y. Zhang, Y. Ma, H. Hosono, Y. H. Lee, S.-G. Kim, S. W. Kim, *Nat. Commun.* **2020**, *11*, 1526.  
[14] K. Huang, *Statistical Mechanics*, 2nd Ed., John Wiley & Sons, New York **1987**.  
[15] A. Arrott, *Phys. Rev.* **1957**, *108*, 1394.  
[16] V. Taufour, D. Aoki, G. Knebel, J. Flouquet, *Phys. Rev. Lett.* **2010**, *105*, 217201.  
[17] T. Misawa, Y. Yamaji, M. Imada, *J. Phys. Soc. Jpn.* **2008**, *77*, 093712.  
[18] T. Misawa, Y. Yamaji, M. Imada, *J. Phys. Soc. Jpn.* **2009**, *78*, 084707.  
[19] D. Bosch, F. Pobell, P. Kienle, *Phys. Lett.* **1966**, *22*, 262.  
[20] V. Gotthardt, H. S. Möller, R. L. Mössbauer, *Phys. Lett. A* **1969**, *28*, 480.  
[21] R. V. Parish, *The Interpretation of <sup>119</sup>Sn-Mössbauer Spectra*, Wiley Interscience, New York **1972**.  
[22] C. L. Seaman, M. B. Maple, B. W. Lee, S. Ghamaty, M. S. Torikachvili, J.-S. Kang, L. Z. Liu, J. W. Allen, D. L. Cox, *Phys. Rev. Lett.* **1991**, *67*, 2882.  
[23] G. R. Stewart, *Rev. Mod. Phys.* **2001**, *73*, 797.  
[24] P. Gegenwart, Q. Si, F. Steglich, *Nat. Phys.* **2008**, *4*, 186.  
[25] B. Shen, Y. Zhang, Y. Komijani, M. Nicklas, R. Borth, A. Wang, Y. Chen, Z. Nie, R. Li, X. Lu, H. Lee, M. Smidman, F. Steglich, P. Coleman, H. Yuan, *Nature* **2020**, *579*, 51.  
[26] J. Custers, P. Gegenwart, H. Wilhelm, K. Neumaier, Y. Tokiwa, O. Trovarelli, C. Geibel, F. Steglich, C. Pépin, P. Coleman, *Nature* **2003**, *424*, 524.  
[27] C. Bagnuls, C. Bervillier, *Phys. Rev. B* **1985**, *32*, 7209.  
[28] P. Coleman, *Introduction to Many-Body Physics*, Cambridge University Press, Cambridge, UK **2015**.  
[29] S. Wirth, F. Steglich, *Nat. Rev. Mater.* **2016**, *1*, 16066.  
[30] Y. Zhang, H. Lu, X. Zhu, S. Tan, W. Feng, Q. Liu, W. Zhang, Q. Chen, Y. Liu, X. Luo, D. Xie, L. Luo, Z. Zhang, X. Lai, *Sci. Adv.* **2018**, *4*, eaao6791.  
[31] E. Bauer, G. Hilscher, H. Michor, C. Paul, E. W. Scheidt, A. Gribanov, Y. Seropegin, H. Noël, M. Sigrist, P. Rogl, *Phys. Rev. Lett.* **2004**, *92*, 027003.  
[32] B. B. Zhou, S. Misra, E. H. da Silva Neto, P. Aynajian, R. E. Baumbach, J. D. Thompson, E. D. Bauer, A. Yazdani, *Nat. Phys.* **2013**, *9*, 474.

- [33] B. C. Sales, D. Mandrus, R. K. Williams, *Science* **1996**, 272, 1325.
- [34] A. P. Morales, A. Pourret, G. Knebel, G. Bastien, V. Taufour, D. Aoki, H. Yamagami, J. Flouquet, *Phys. Rev. B* **2016**, 93, 155120.
- [35] B. H. Toby, R. B. Von Dreele, *J. Appl. Crystallogr.* **2013**, 46, 544.
- [36] G. Kresse, J. Furthmüller, *Phys. Rev. B* **1996**, 54, 11169.
- [37] P. E. Blöchl, *Phys. Rev. B* **1994**, 50, 17953.
- [38] J. P. Perdew, K. Burke, M. Ernzerhof, *Phys. Rev. Lett.* **1996**, 77, 3865.
- [39] K. Momma, F. Izumi, *J. Appl. Crystallogr.* **2011**, 44, 1272.